

This work was written as part of one of the author's official duties as an Employee of the United States Government and is therefore a work of the United States Government. In accordance with 17 U.S.C. 105, no copyright protection is available for such works under U.S. Law.

Public Domain Mark 1.0

<https://creativecommons.org/publicdomain/mark/1.0/>

Access to this work was provided by the University of Maryland, Baltimore County (UMBC) ScholarWorks@UMBC digital repository on the Maryland Shared Open Access (MD-SOAR) platform.

Please provide feedback

Please support the ScholarWorks@UMBC repository by emailing scholarworks-group@umbc.edu and telling us what having access to this work means to you and why it's important to you. Thank you.

Analysis of Water Vapor Correction for CloudSat W-Band Radar

D. Josset, S. Tanelli, Y. Hu, J. Pelon, and P. Zhai

Abstract—We analyzed different models to estimate absorption at W-band by gaseous species by taking advantage of the collocated CloudSat–Cloud-Aerosol Lidar and Infrared Pathfinder Satellite Observation (CALIPSO) measurements. We used the power backscattered by the surface in the green visible wavelength of the lidar of CALIPSO as a reference to infer CloudSat’s 94-GHz ocean surface backscatter in clear air and infer the attenuation introduced by gaseous absorption. Different millimeter-wave propagation models (MPMs) and different sources to determine the profile of atmospheric thermodynamic state are used to estimate CloudSat attenuation. These estimates are compared to the observations to calculate the residual dispersion. We show here that we need to adjust the empirical constants of preexisting water vapor absorption models to minimize the dispersion. Our results indicate an overestimation of absorption by the water vapor continuum at 94 GHz in Liebe-based MPM. We also propose a new empirical model to better represent the absorption of the water vapor continuum near 94 GHz. When this model is used in combination with the Advanced Microwave Scanning Radiometer for the Earth Observing System water vapor path and the Global Modeling and Assimilation Office water vapor vertical profile distribution, it leads to the lowest dispersion of the data on a statistical basis (global data over one month). The improved model is expected to optimize water vapor correction applied to CloudSat data and, potentially, also to improve interpretation of brightness temperature measurements in the W-band (e.g., 85- and 98-GHz radiometric channels).

Index Terms—Laser radar, radar, remote sensing, water vapor.

NOMENCLATURE

CALIPSO	Cloud-Aerosol Lidar and Infrared Pathfinder Satellite Observation.
CPR	Cloud Profiling Radar.
AMSRE	Advanced Microwave Scanning Radiometer for the Earth Observing System.

Manuscript received April 2, 2012; revised August 24, 2012 and October 12, 2012; accepted November 8, 2012. Date of publication January 30, 2013; date of current version June 20, 2013. This work was supported by NASA, CNES and Science System and Applications, Inc. in the frame of the CALIPSO mission.

D. Josset and P. Zhai are with Science Systems and Applications, Inc., Hampton, VA 23681 USA (e-mail: damien.b.josset@nasa.gov; pengwang.zhai-1@nasa.gov).

S. Tanelli is with the Radar Science and Engineering Section, Jet Propulsion Laboratory, California Institute of Technology, Pasadena, CA 91109 USA (e-mail: simone.tanelli@jpl.nasa.gov).

Y. Hu is with the Atmospheric Composition Branch, Langley Research Center, National Aeronautics and Space Administration, Hampton, VA 23681 USA (e-mail: yongxiang.hu-1@nasa.gov).

J. Pelon is with the Laboratoire Atmosphères, Milieux, Observations Spatiales, Université Pierre et Marie Curie/Institut Pierre-Simon Laplace/Centre National de la Recherche Scientifique, 75252 Paris, France (e-mail: jacques.pelon@latmos.ipsl.fr).

Color versions of one or more of the figures in this paper are available online at <http://ieeexplore.ieee.org>.

Digital Object Identifier 10.1109/TGRS.2012.2228659

MPM	Millimeter-wave propagation model.
ECMWF	European Centre for Medium Range Weather Forecast.
GMAO	Global Modeling and Assimilation Office. In this paper, it relates to the thermodynamical inputs coming from the ancillary meteorological data provided by the GMAO.
GAMSRE	Acronym used when the GMAO humidity profiles are adjusted to the integrated water vapor path (IWVP) of AMSR-E.
GMODIR	Acronym used when the GMAO humidity profiles are adjusted to the IWVP of the MODerate-resolution Imaging Spectroradiometer (MODIS) infrared product.
MPM85	Model of Liebe version of 1985.
MPM85*	Model of Liebe “reduced” version of 1985 containing only the main absorption lines.
MPM85*CO	Model of Liebe version of 1985. “Reduced” variant to improve computation speed but including a correction term to take into account the removal of absorption lines.
MPM93	Model of Liebe version of 1993. Standard version parameterizing the water vapor continuum with an absorption line at 1780 GHz.
MPM93L1	Model of Liebe version of 1993. Variant using the 1470-GHz absorption line instead of the standard 1780 GHz.
MPM93L2	Model of Liebe version of 1993. Variant using the 2200-GHz absorption line instead of the standard 1780 GHz.
MPM93*	Model of Liebe version of 1993. Standard for the continuum (absorption line at 1780 GHz) but “reduced” model containing only the main absorption lines.
LIROS	Model of Liebe version of 1993 but the water vapor continuum is parameterized with the self- and foreign-broadened expressions of Rosenkranz and not with a line in the terahertz region (1780 GHz).
LIROS*	“Reduced” version of the LIROS model containing only the main absorption lines.
LIROMA	Model of Liebe version of 1993 but the water vapor continuum is parameterized with the self-broadened expression of Rosenkranz and the foreign-broadened expression of Ma and Tipping instead of using a line in the terahertz region (1780 GHz).

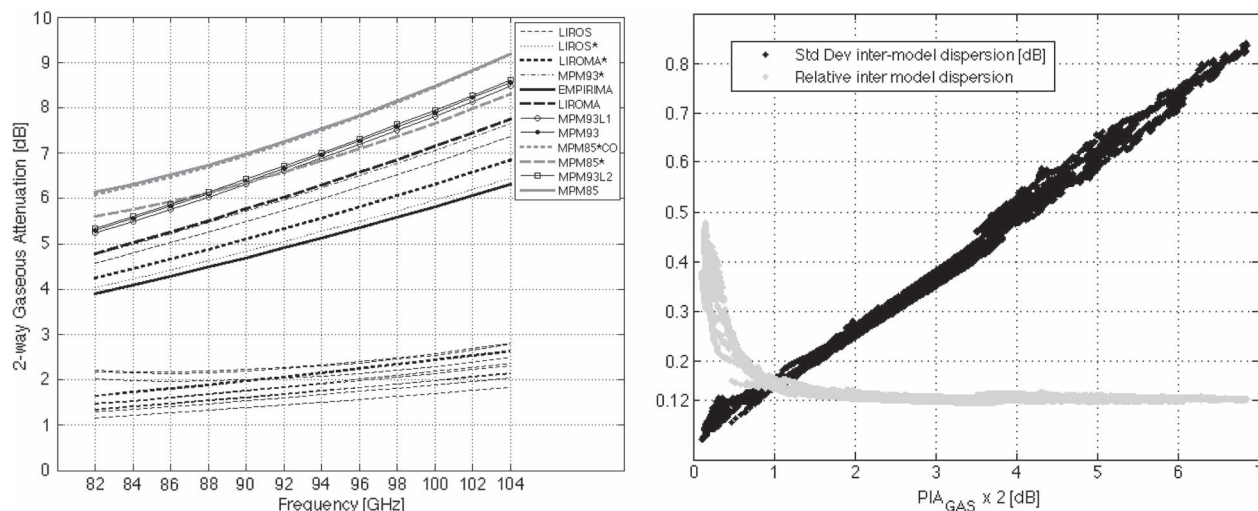


Fig. 1. (Left) Total two-way PIA due to gaseous absorption calculated by a set of models (acronyms defined in Section II-B) over the range of frequencies encompassing the typical remote sensing channels in W-band. Two sets of curves derived from two sample ECMWF profiles: The top set (with total values in the 4–8-dB range) derives from a profile sampled in daytime at 10° N, 168° E with a total column of 57 mm of water vapor and a surface temperature of 26°C; the lower set (total values ranging between 1 and 3 dB) derives from a profile sampled in nighttime at 34° S, 6° E. The legend applies only to the top set; curves of the lower set are indifferiated. (Right) Ensemble of PIA calculations (one for each of the models) performed over one sample CloudSat orbit. The standard deviation and average of the ensemble are calculated for each of the about 36 000 profiles: The latter is used for the *x*-axis, the former is the black plots, and their ratio is the grey dots. The spread of the ensemble scales well with the amplitude of the PIA.

LIROMA*	“Reduced” version of the LIROMA model containing only the main absorption lines.
Operational	Gaseous attenuation from CloudSat operational product.
TAN	Correction based on a linear function of AMSRE IWVP developed by Tanelli and coauthors.
EMPIRIMA	Model of Liebe version of 1993 but the water vapor continuum is parameterized with the foreign-broadened expression of Ma and Tipping and the self-broadened continuum expression of Rosenkranz is reduced by half, which minimizes the dispersion in our study.
NOCORR	No correction is applied to CloudSat data.

I. INTRODUCTION

THE CLOUDSAT mission embarks the first W-band (i.e., 94 GHz) spaceborne radar [1]. This frequency is an optimal choice to achieve the required sensitivity in cloud, but it is affected by significant attenuation. In the presence of liquid water or dense frozen hydrometeors, the signal is affected so that the useful portion of the profile does not extend all the way to the surface, but even in the absence of condensate, atmospheric attenuation due to gaseous species (mainly water vapor absorption) results in two-way attenuation up to 8 dB in the tropics (i.e., ~85% of the signal is attenuated). This effect has to be corrected to derive an unbiased measure of radar reflectivity. On one hand, Correction of Gaseous Attenuation (CGA) affects the absolute external calibration of the radar system which is achieved by comparing the observed surface backscatter in clear air to the expectation derived from physical and empirical models (see [1] and the references therein for a complete discussion). On the other hand, the same correction is embedded in the processing chain of the CloudSat products

(in particular, in the L2B-GEOPROF product, whence all other Level 2 and 3 products stem from).

In the operational product analysis (R04), the CloudSat CGA is based on the MPM of Liebe [2]. Several versions of this model exist (e.g., [3] and [4]) and were used by different authors [5]–[8]. The choice of a given MPM is not without consequences as it can create a significant bias in the geophysical parameters retrieved from microwave observations like the column liquid water path [9], and the evaluation of the accuracy of the different MPM is still an active subject of research [10], [11]. The inputs to MPM in R04 are vertical profiles of temperature and water vapor density obtained from ECMWF global reanalysis data. At these frequencies, attenuation is determined mainly by the background continuum and line shapes of the prevailing species (N₂ and O₂ in particular) and by the water vapor lines which are modulated by the water vapor vertical profile of concentration.

Fig. 1 shows that the CGA implemented with different MPMs (see Section II-B) carries, in general, a root-mean-square variation of approximately 12%. In the tropics, this corresponds to a 0.8-dB intermodel standard deviation. Since this is a model-dependent error, it will manifest itself as a bias.

While these amounts are within the budgeted absolute calibration accuracy of CloudSat (see [1]), they present the undesirable character of being correlated to other quantities of interest (i.e., temperature and humidity). It would be irresponsible to preserve them if we have the means to reduce them. Furthermore, besides affecting the assessment of the overall calibration of the instrument, any residual noncompensated attenuation affects all the retrievals obtained from the CPR measurements. For example, the PRECIP-COLUMN product [12] is based primarily on the estimates of path-integrated attenuation (PIA) due to precipitation. Among the sources of uncertainty that affect the estimates of PIA, one is uncompensated (or overcompensated) gaseous attenuation. Its impact on the final retrieval

depends on the rain intensity and layer thickness (see [12]). In general, it is more significant for shallow light rain, which is exactly the type of precipitation where the CloudSat mission has covered an existing observational gap. A simplified example can provide a measure of the resulting errors in the retrievals: If we assume an uncompensated amount of 0.5 dB of gaseous attenuation affecting a measurement taken over a 1-km-thick precipitation layer of 1 mm/h, the resulting error in precipitation rate retrieval is on the order of 25%. This quantity is mitigated by the methods implemented in the algorithm to estimate the PIA, and it is mixed with other sources of error. Nevertheless, contrary to most other sources of error, this one is correlated to the local atmospheric state variables, a particularly undesirable trait.

Discerning which model performs best at the CloudSat frequency has been the matter of prior analyses which could not however rely on the accuracy provided by the CloudSat/CALIPSO data set ([13] and [14]) and the method discussed here.

The goal of the present study is to determine which water vapor absorption model offers the most accurate correction based on the analysis of surface echo as a common CloudSat–CALIPSO reference and what should be the thermodynamical inputs used for this model.

The uncorrelated error sources present in the lidar and radar ocean surface observations allow us to achieve this goal. We use different ways to correct CloudSat gaseous attenuation and select the one offering the lowest dispersion. In this framework, we used the water vapor product of the MODIS [15] and that of the AMSR-E [16], as well as the GMAO products, as alternative inputs for the water vapor correction.

In the second part, we describe the general underlying principle of our methodology, the different characteristics of the models that we used to correct water vapor absorption, their main differences, and the different thermodynamical inputs. We also describe the specificity of our analysis using CALIPSO and CloudSat data. In the third part, we discuss our results using those different models and the water vapor input retrieved by AMSR-E, MODIS, and the GMAO model. We will finish with a few conclusive words and perspectives.

II. METHODOLOGY

A. Reference Provided by the Lidar Optical Measurements

In order to determine the accuracy of CloudSat water vapor correction, a reference has to be found. If this reference is not totally stable and is affected by errors, those errors must be uncorrelated as much as possible to the error sources affecting the radar measurements and to the error sources affecting MPM and its inputs. The reference selected in this work is the lidar measurement of oceanic backscattering cross section obtained by CALIPSO. CloudSat and CALIPSO have been flying in close formation within the A-train from their launch in April 2006 until April 2011; during this period, more than 90% of the measurements have been collocated in space and acquired within 20 s from each other. We have shown in our previous studies [15], [16] that a relationship exists between the radar- and lidar-measured oceanic scattering cross sections. Indeed,

the ocean surface has a given roughness and refractive index, which results into different cross sections at the two measurement wavelengths.

Following [16], the lidar backscatter normalized cross section γ_{SL} (in per steradian; subscript S for surface and L for lidar) can be expressed as

$$\gamma_{SL} = \frac{C_L \rho_L}{4\pi \langle S^2 \rangle_L} T_L^2. \quad (1)$$

The radar normalized cross section σ_{SR} (no unit; subscript R for radar; note that, contrary to common practice in radar, we have opted to express σ_{SR} always in linear space and not in decibels) can be expressed by a similar expression

$$\sigma_{SR} = \frac{C_R \rho_R}{\langle S^2 \rangle_R} T_R^2. \quad (2)$$

$\langle S^2 \rangle_{R,L}$ is the variance of the slope distribution of the waves formed at the surface by wind stress commonly called mean square slope. $\rho_{R,L}$ is the Fresnel reflectance coefficient. Variations of ρ_R with sea surface temperature (SST) have been taken into account using [17] and AMSR-E SST measurement with a constant—35‰—salinity as input. For lidar, ρ_L can be considered constant and equal to 0.0213 at 0.53 μm [18]. $C_{R,L}$ and $\langle S^2 \rangle_{R,L}$ take into account the diffraction induced by the size of the scattering elements linked to surface waves with respect to the measurement wavelength and the spectral cut [5], [19], [20]. For lidar measurements, as the wavelength is much smaller than the capillary waves, C_L only represents the reflectance modification due to foam and bubble formation at wind speed larger than 10 m/s [21]–[23]. $T_{R,L}^2$ is the two-way atmospheric transmission at radar (lidar) wavelength.

For a given state Ω_{SS} (subscript SS for sea surface) of the ocean roughness, there are unique values of the observed lidar and radar signals (γ_{SS} and σ_{SS}) if the influence of water temperature and salinity (on Fresnel coefficient) and atmospheric attenuation has been accurately corrected. For the CALIPSO and CloudSat data, we perform this correction, and the corresponding expressions are

$$\gamma_{SS} = \gamma_{SL} (C_L, T_L^2 = 1) \quad (3)$$

$$\sigma_{SS} = \frac{0.4\sigma_{SR}}{\rho_R T_R^2}. \quad (4)$$

Supplemental details to derive these expressions from the operational products are provided in Section II-D.

The end result is naturally affected by the measurement and model errors, and the observed values of the lidar and radar signals γ_{obs} and σ_{obs} can be written as

$$\gamma_{\text{obs}}(\Omega_{SS}) = \gamma_{SS}(\Omega_{SS}) + \Delta\gamma_{SS}(E_{L1}, \dots, E_{LN}). \quad (5)$$

E_{LN} represents the different sources of error on the lidar measurement; they are due to the lidar energy correction, instrumental noise, and aerosol attenuation variation in the clearest conditions, the “baseline” [24].

For the radar, the equivalent expression is

$$\sigma_{\text{obs}}(\Omega_{SS}) = \sigma_{SS}(\Omega_{SS}) + \Delta\sigma_{SS}(E_{R1}, \dots, E_{RN}) \quad (6)$$

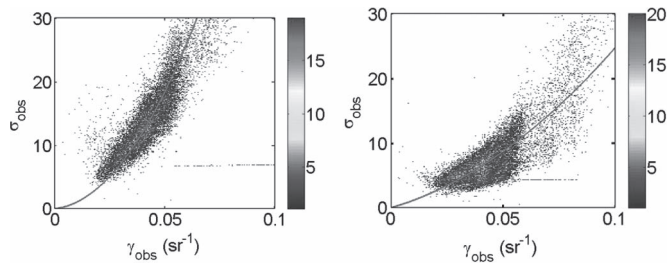


Fig. 2. Radar surface echo as a function of the lidar surface echo. Color code is the number of occurrences. (Left) Correction by MPM93 using AMSR-E IWVP as input. (Right) No correction is applied to CloudSat data (nighttime data in August 2006). The solid line represents the second-order polynomial best fit (least squares sense) forced to go through the origin.

Where E_{RN} terms represent the radar error sources. We will define them as E_{CGA} , E_{H_2O,O_2} , $E_{SST,Salinity}$, and E_{inst} , which are the error coming from the water vapor and oxygen absorption model used in the MPM, the error coming of atmospheric thermodynamical properties (water vapor and dry air profile) used as MPM input, the error on radar Fresnel reflectance model used, and all the radar instrumental errors, respectively. One can note that the error sources are different for the radar and lidar and the variations of (5) and (6) are therefore uncorrelated. The errors for lidar data have been discussed previously [15], [16]. This study focuses on minimizing the first two error terms (E_{CGA} and E_{H_2O,O_2}) in the radar data analysis. The observed value of the radar signal for a given state of the ocean can be found in the neighborhood of a given value of the lidar signal (within a small variation $\Delta\gamma$). This can be written as

$$\frac{1}{2\Delta\gamma} \int_{\gamma_{SS}(\Omega_{SS})-\Delta\gamma}^{\gamma_{SS}(\Omega_{SS})+\Delta\gamma} \sigma_{obs}(\gamma_{SS}) d\gamma_{SS} = \sigma_{obs}(\Omega_{SS}). \quad (7)$$

Fig. 2 shows the σ_{obs} as a function of γ_{obs} . Radar signal is shown uncorrected and corrected using the model of Liebe 1993 and GMAO pressure and humidity profile scaled to have the IWVP retrieved by AMSR-E. The data are those obtained during nighttime of August 2006 with R04 version. As we can see, water vapor correction reduces significantly the data dispersion. As expected, the water vapor correction not only modifies the shape of the average empirical relationship, which can be determined from the data, but also allows one to drastically reduce the dispersion around it. The core of this study is the analysis of this dispersion using various corrections. In this paper, dispersion has to be understood as the statistical dispersion, which is the variability or spread of σ_{obs} introduced by measurement and model errors as expressed by (6) and (7). Usual measures of the dispersion include the standard deviation and the interquartile range (IQR), and the formalism that we have used is explained in Section II-D.

B. Liebe's MPM

The different versions of Liebe's MPM [2]–[4] can predict attenuation, delay, and noise properties of moist air for microwave and frequencies up to 1000 GHz. They use the height

distribution of pressure, temperature, and humidity along the radio path to calculate the absorption lines of H_2O and O_2 at different frequencies and the associated moist air complex refractive index. The internal variables are the dry air pressure p , partial pressure of water vapor e , and the reciprocal temperature $\theta = 300/T$ (T being the temperature in kelvins). The inputs are profiles of relative humidity, temperature, and pressure, which can be measured by dropsondes and radiosondes launched from plane [5] or from the surface, or provided by a model, ECMWF in the operational product [1] or GMAO [16]. The Bolton formula has been used for all models to retrieve the saturation water vapor pressure (see Appendix B for more details).

A few refinements have been performed on the number of oxygen and water vapor absorption lines as well as their shape between different versions of MPM. However, the main difference is coming from the treatment of the so-called water vapor continuum which is treated in an empirical way to best fit the observations. MPM85 [3] and MPM93 [4] are particularly interesting as several versions for each of them are provided and can be used to test the sensitivity of the model to small modifications. A reduced model MPM85* uses only the main absorption lines to improve computer time under 300 GHz. For MPM93, the water vapor continuum is parameterized in term of a water vapor pseudoline in the terahertz region and proposes three different parameterizations of this line. Those models have since been updated by Rosenkranz [25], [26]. Theoretical developments of the H_2O-N_2 collision process allowed one to further refine the water vapor continuum expression [27].

The different models and the denomination that we used are described as follows.

- 1) Liebe's model 1985 [3] is referred to as MPM85.
- 2) The reduced version of the same model is referred to as MPM85*.
- 3) The reduced version using the correction term suggested by Liebe [3] is referred to as MPM85*CO.
- 4) Liebe's model 1993 [4] is referred to as MPM93.
- 5) The same model using the 1470-GHz line instead of the suggested 1780 GHz is referred to as MPM93L1.
- 6) The same model using the 2200-GHz line instead of the suggested 1780-GHz line is referred to as MPM93L2.
- 7) The same model but reduced using only the lines used in MPM85* and the 1780 GHz for water vapor continuum is referred to as MPM93*.
- 8) Liebe's model 1993 [4] but the 1780-GHz line (vapor continuum) is replaced by the self- and foreign-broadened continuum expression in [25] and [26]. The expression of the continuum in the paper of Rosenkranz [25], [26] is coming from the model of Liebe but modified to be used with a different line shape which incorporates a frequency cutoff and a subtracted baseline as given by [28]. As explained in [25], when the Van Vleck–Weisskopf line shape is used, 3% has to be subtracted from the self-broadened, and 15% has to be subtracted from the foreign-broadened contribution. This model is referred to as LIROS.
- 9) The same model but using only the lines of MPM85* is referred to as LIROS*.

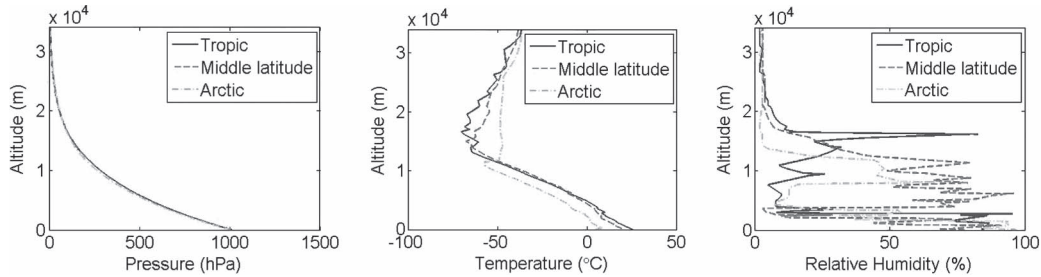


Fig. 3. Pressure, temperature, and relative humidity profiles for the three radio soundings described in Section II-B, illustrative of arctic, middle latitude, and tropical conditions.

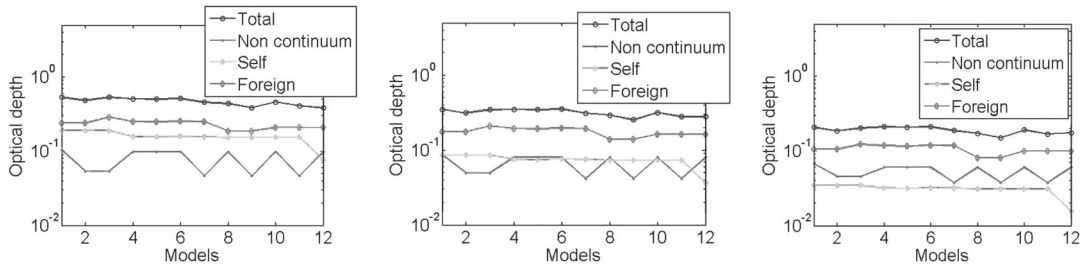


Fig. 4. Optical depth of the different MPM using the three radio-sounding profiles shown in Fig. 3 as inputs and separated by their different contributions (see Section II-B). (Left) Tropics. (Middle) Middle latitude. (Right) Arctic. Models 1 to 11 correspond to the list in Section II-B. Model 12 is the one called EMPIRIMA.

- 10) The same model as LIROS but the foreign-broadened expression is replaced by the parameterization in [27]. This model is referred to as LIROMA.
- 11) The same model but using only the lines of MPM85* is referred to as LIROMA*.
- 12) The gaseous attenuation from CloudSat operational product is called operational.
- 13) The correction based on a linear function of AMSR-E IWVP [1] is called TAN.
- 14) We modified the model of Liebe 93 and used the foreign-broadened parameterization in [27]; we then adjusted the self-broadened parameterization in [25] in order to obtain the lowest dispersion (see Annex A). This model is referred to as EMPIRIMA. The idea behind this model is that the parameterization in [25] is already an empirical adjustment which can be further improved.
- 15) When no correction of CloudSat data is performed, we call it no correction (NOCORR).

To better illustrate the differences between the models that we are using in this study, we are showing in Fig. 3 the atmospheric conditions (pressure, temperature, and relative humidity) for three atmospheric radio-sounding profiles taken on August 15, 2006 at 12Z. One radio sounding was taken at tropical latitudes (21.98° N, 159.35° W) from PHLI Lihue station, one at middle latitudes (43.93° N, 60.01° W) from WSA Sable Island station, and one in the arctic latitudes (71.30° N, 156.78° W) from PABR Barrow station. For those three radio soundings, the amounts of precipitable water vapor are 1.44 cm in the arctic, 2.87 cm in the middle latitudes, and 3.64 cm in the tropics.

Those radio soundings are interpolated on the same grid and used as thermodynamical inputs of the different MPM

previously described. The associated atmospheric optical depth is shown in Fig. 4. Models 1 to 11 follow the numbering of the list of the previous paragraph (MPM85 to LIROMA*), and number 12 is EMPIRIMA. We separated the optical depth into different components: Total is the total attenuation, noncontinuum is the total attenuation but with the continuum removed, self is the continuum when the dry air pressure is set at zero, and foreign is the difference between continuum and self. The optical depth differences are mainly linked to the different water vapor content.

C. Thermodynamical Inputs Used for the Models

The different inputs used to test the MPMs are the following.

- 1) We forced GMAO humidity profiles used in CALIPSO data analysis to be adjusted to the IWVP from AMSR-E with a multiplicative constant. We call this input GAMSRE.
- 2) Same thing with MODIS infrared IWVP. We call this input GMODIR.
- 3) GMAO alone is called GMAO.

Those thermodynamical inputs are used with the models described in Section II-B with the exception of Operational (which is precalculated), TAN (which does not require a profile), and NOCORR (no inputs are necessary).

For CloudSat water vapor operational correction, it is important to note that we can only use the maximum of the attenuation profile at the last usable range bin which is calculated several hundred meters above the sea surface. It is much higher than the lowest data point in the ECMWF model (at 1000 hPa). As there is an important amount of moisture in the lower part of the atmosphere and within the boundary

layer, one should note that the water vapor content is then seriously underestimated when we are using the Operational correction (see Section III for supplemental discussions). The high altitude of the last usable range bin makes it impractical for a simple correction procedure like an extrapolation of the data at the surface level, and this issue is at least partially related to CloudSat data formatting procedures. We are currently conducting supplemental work looking for the appropriate interpolation of the ECMWF model at the surface level. The same problem arises but to a lesser extent when GMAO is used alone as a thermodynamical input (GMAO). GMAO profiles, as reported in the CALIPSO files, are composed of 33 fixed altitude levels with a resolution of around 1 km near the surface level (the bin closest from the surface being at an altitude of around 60 m). To correct this effect, the position of the surface level in the model is extended (or shortened) to match the altitude where the CALIPSO surface level is. The thermodynamical variables (pressure, temperature, and humidity) are modified accordingly by a linear interpolation. We expect this procedure to reduce the uncertainty by using the finer resolution (30 m) of the CALIPSO vertical profile. We are using the same profile shape for the three thermodynamical inputs (GAMSRE, GMODIR, or GMAO) in order not to create an inconsistency between the different inputs. However, using or not the surface extension procedure is not a necessity when the water vapor profile is adjusted to the IWVP of AMSR-E and MODIS (for GAMSRE and GMODIR corrections). The scope of this study is limited to the use of model data already included in the satellite products. However, it is important to note that not all GMAO data fields are reported into the CALIPSO files and the model contains supplemental surface information on pressure and humidity which could be used as complementary inputs of the CGA procedure.

D. Application to Lidar and Radar Data Analyses

We present here the results for one month (August 2006) of observations of the ocean surface over the globe using CloudSat Level 1 Release 04, CALIPSO Level 1 version 3 data, AMSR-E ocean product version 5, and MODIS Level 2 collection 005. To meet the low attenuation condition of (3) ($T_L^2 = 1$), only the clearest cases with lidar integrated attenuated backscattering coefficient γ_{atmL} lower than 0.01 sr^{-1} [16] have been selected. In fact, while clear air should be strictly defined as moist air with no presence of matter in solid or liquid phase, such conditions, strictly speaking, never occurred on Earth; however, the limit on the lidar backscattering coefficient described previously guarantees that any attenuation due to scattering by particles does not create correlated variations in the lidar and radar signals and can be neglected.

The lidar atmospheric attenuation by molecular air is then corrected using GMAO density profile and ozone concentration. Whether or not we correct ozone attenuation does not seem to affect the result of this study, probably because of its overall low effect on the lidar signal and the lack of correlation with the other lidar error sources. However, this correction allows us to simplify the discussion as we are closer from the condition $T_{R,L}^2 = 1$, as described in (3). The C_L coefficient

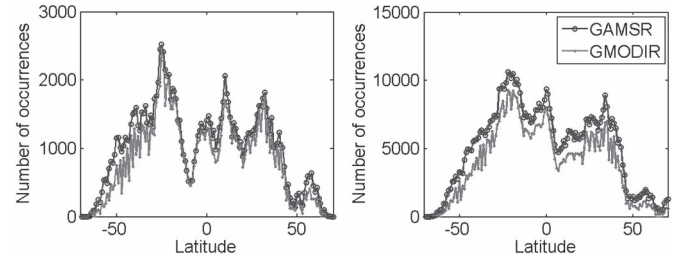


Fig. 5. (Left) Nighttime data (August 2006): latitudinal distribution of the number of observations in our analysis when AMSR-E (GAMSRE) or MODIS (GMODIR) is used. (Right) Same picture for daytime data (August 2006).

has been shown to be stable between 3 and 10 m/s [16], so in our analysis, γ_{obs} variation range has been limited to the corresponding values of 0.0285 and 0.056 sr^{-1} to meet the second condition of (3) ($C_L = 1$).

When scaling the radar surface signal at global scale, the ocean temperature dependence of the refractive index needs to be taken into account [1], and as previously mentioned, ρ_{0R} variations with SST (negligible for ρ_{0L}) have been taken into account.

Only valid estimates of AMSR-E IWVP and SST are kept in the analysis. As the invalid data point in AMSR-E data format is around 255, thresholds of 150 kg/m^2 and 150°C have been used to exclude anomalous data points. As AMSR-E is used to correct water temperature variations and to preserve fairness in the comparisons, only points with available AMSR-E SST measurements are retained also when GMAO-only or the operational product is used for correction. When MODIS measurements are used, only the subset including valid AMSR-E SST measurements is taken into account. Comparisons of the three distributions do not show specific structures that would indicate that there is a bias in the number of MODIS observations toward places of high or low water vapor content. Fig. 5 shows the number of observations used in the analysis for GAMSRE and GMODIR. As we can see, GMODIR is a subset of GAMSRE with a similar distribution of the data.

Furthermore, points where σ_{obs} exceeded 150 ($\sim 22 \text{ dB}$) have been suppressed. Such large values are often associated with extremely low winds and presence of coherent (i.e., specular) contributions to the backscatter which are not captured by the models adopted here and which often result in saturation at the receiver, hence deteriorating any relation between radar and lidar measurements.

CloudSat and CALIPSO collocated data are reported on a grid with resolutions $\Delta\gamma = 5.10^{-4} \text{ sr}^{-1}$ (for the lidar signal) and $\Delta\sigma = 10^{-2}$ (for the radar). The choice of these resolutions is driven by the size of the data set (one month); using a longer time period would allow one to enhance this resolution, but it may introduce other sources of error (e.g., calibration and sensitivity change of the instruments with time, and stratospheric aerosol load variations). As γ_{obs} values are between 0.0285 and 0.056 sr^{-1} , the small interval condition of (7) is met by $5.10^{-4} \text{ sr}^{-1}$.

If we refer to index i for γ_{obs} and j for σ_{obs} , the total number of grid points in each dimension is n_i and n_j . The number of data per grid point is $N(\gamma_i, \sigma_j)$. In order to analyze the

dispersion of the data in terms of relative error, for a given i (and γ_i), the central tendency of σ_{SS} has to be determined. We use the median (subscript m for median) value of radar cross section $\sigma_m = \sigma_{\text{obs}}(m(\gamma_i))$, where index $m(\gamma_i)$ correspond to the median along one dimension of the distribution and is defined as

$$\sum_{j=1}^{j=m(\gamma_i)} N(\gamma_i, \sigma_j) = \frac{1}{2} \sum_{j=1}^{n_j} N(\gamma_i, \sigma_j). \quad (8)$$

We used the median value as the central tendency of the distribution. Following (6), we can then write $\sigma_m = \sigma_{SS}$. For each value of γ_i , σ_{obs} is divided by σ_m in order to obtain the associated dispersion $\Delta\sigma_{SS}/\sigma_m$. As the grid step is also divided by σ_m (and σ_m mean value is around ten, as can be seen in Table II), the new data sample is reported on a 10^{-3} grid for the radar. Since this dispersion is not a function of γ_i , we can perform a mean of this dispersion for all γ_i to increase the number of available observations and statistical meaningfulness of our analysis. Doing so and subtracting one, we obtain a distribution of the relative error centered on zero with a mean number $\nu(\Delta_j)$ of the data repartition. Δ_j is the index of the 1-D grid corresponding to the overall dispersion. $N\Delta_j$ is the total number of grid points. The IQR of the distribution is then calculated to obtain a quantification of the dispersion.

More precisely, we determine indices $Q1$ and $Q3$ of the first and third quartiles of the average distribution as

$$\sum_{j=1}^{j=Q1} \nu(\Delta_j) = \frac{1}{4} \sum_{j=1}^{N\Delta_j} \nu(\Delta_j) \quad (9)$$

$$\sum_{j=1}^{j=Q3} \nu(\Delta_j) = \frac{3}{4} \sum_{j=1}^{N\Delta_j} \nu(\Delta_j) \quad (10)$$

which give the IQR on radar cross sections as

$$\text{IQR} = \sigma_{\text{obs}}(\Delta_{Q3}) - \sigma_{\text{obs}}(\Delta_{Q1}). \quad (11)$$

We chose the IQR for our criteria of dispersion as it is robust and insensitive to the skewness of the distribution. As we will show, using the standard deviation leads to the same overall conclusions, but in that case, one should also discuss the different moments (or at least the skewness) of each distribution. Considering the high number of data points, the central limit theorem applies when water vapor attenuation is well corrected. However, the distribution can show a high skewness, for example, when no correction is used. In that case, IQR remains a good parameter of the data dispersion and allows meaningful and consistent comparisons with distribution showing different skewness. Fig. 6 shows the data distribution $\nu(\Delta_j)$ when no correction of water vapor absorption is applied to CloudSat data, considering all classes of lidar data γ_i . This leads to the dispersion of the distribution along the dimension of Δ_j index. IQR is the interval between the two solid lines. It is close to 0.4, and one can notice that the distribution is far from Gaussian. For comparison, we are showing in Fig. 7 the data distribution when CloudSat operational water vapor correction is used. As we can

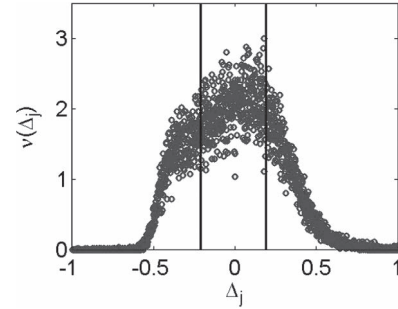


Fig. 6. Distribution of the CloudSat data after treatment, showing the relative dispersion when no correction is applied. IQR is the distance between the two vertical solid lines.

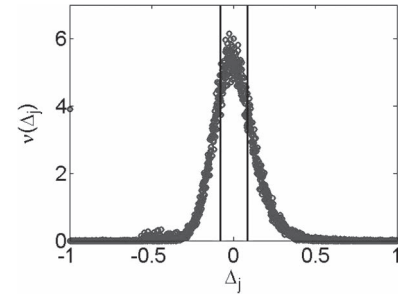


Fig. 7. Same as Fig. 6 but using the operational CloudSat water vapor correction.

see, the dispersion decreases, and the distribution has an aspect closer from a Gaussian distribution with an IQR of around 0.17.

III. DISCUSSION

The domain of validity of the different versions of Liebe's MPM covers an important range of frequencies going from 1 to 1000 GHz. For the use at a single wavelength, the accuracies of the different versions can be examined one by one. Table I (and Table III) shows the dispersion in terms of IQR for the different versions of MPM and different inputs for nighttime (and daytime) data. Given the binning strategy described in Section II-D (original quantization is 0.01 and further scaling by about 1/10), the results in Table I have a significance of ± 0.001 . Table II (and Table IV) shows the mean value of σ_m for the same data used to study the dispersion for nighttime (and daytime) data. The numbers of data used for the statistic are around 100 000 for nighttime and 500 000 for daytime. There is more noise in the lidar measurements during daytime; this explains the higher number of observations below the "clear air" threshold. This higher noise does not affect our methodology, and as we will see, the results do not change significantly for daytime. The standard deviation of the Gaussian distribution that best fits the data distribution in the least squares sense is also provided for reference.

Several general tendencies can be seen, and it is interesting to observe such a straightforward behavior of the dispersion: When a model is better, it is better whatever the thermodynamical input is. It is slightly different for the thermodynamical input, but when an input is better, it is, in general, better for most of the models. We are discussing results for nighttime data only. Thermodynamic parameters are different during daytime, so as we can see in Tables I–IV, the number between nighttime

TABLE I
RELATIVE DISPERSION (IQR) OF THE NIGHTTIME DATA USING DIFFERENT MODELS AND DIFFERENT WATER VAPOR INPUTS. LOW DISPERSION VALUES ARE IN BOLD. THE STANDARD DEVIATION OF THE DISTRIBUTION IS INDICATED FOR REFERENCE IN PARENTHESES

IQR	GAMSRE	GMODIR	GMAO
MPM85	0.258(0.196)	0.280(0.211)	0.244(0.184)
MPM85*	0.212(0.159)	0.248(0.186)	0.201(0.149)
MPM85*CO	0.258(0.196)	0.280(0.212)	0.243(0.184)
MPM93	0.233(0.175)	0.262(0.196)	0.222(0.166)
MPM93L1	0.227(0.170)	0.258(0.196)	0.217(0.164)
MPM93L2	0.236(0.177)	0.265(0.199)	0.225(0.170)
MPM93*	0.190(0.141)	0.232(0.173)	0.184(0.137)
LIROS	0.183(0.135)	0.225(0.168)	0.177(0.132)
LIROS*	0.161(0.117)	0.202(0.150)	0.159(0.117)
LIROMA	0.192(0.143)	0.234(0.174)	0.186(0.139)
LIROMA*	0.165(0.121)	0.208(0.154)	0.162(0.118)
Operational	0.166(0.121)		
TAN	0.210(0.156)		
EMPIRIMA	0.157(0.115)	0.195(0.144)	0.159(0.116)
NOCORR	0.402(0.361)		

TABLE II
MEAN VALUE OF THE NIGHTTIME DATA USING DIFFERENT MODELS AND DIFFERENT WATER VAPOR INPUTS

σ_m	GAMSRE	GMODIR	GMAO
MPM85	14.10	15.15	13.77
MPM85*	13.07	13.92	12.80
MPM85*CO	14.02	15.06	13.69
MPM93	13.79	14.74	13.47
MPM93L1	13.69	14.62	13.38
MPM93L2	13.86	14.83	13.53
MPM93*	12.74	13.50	12.47
LIROS	12.34	13.06	12.09
LIROS*	11.39	11.95	11.19
LIROMA	12.85	13.62	12.57
LIROMA*	11.86	12.48	11.63
Operational	11.85		
TAN	13.43		
EMPIRIMA	11.66	12.18	11.47
NOCORR	6.78		

TABLE III
SAME AS TABLE I BUT FOR DAYTIME DATA

IQR	GAMSRE	GMODIR	GMAO
MPM85	0.223(0.158)	0.287(0.205)	0.219(0.157)
MPM85*	0.192(0.135)	0.259(0.185)	0.190(0.133)
MPM85*CO	0.223(0.158)	0.286(0.204)	0.219(0.157)
MPM93	0.204(0.145)	0.272(0.193)	0.204(0.145)
MPM93L1	0.201(0.142)	0.270(0.191)	0.201(0.142)
MPM93L2	0.207(0.147)	0.275(0.196)	0.207(0.147)
MPM93*	0.179(0.125)	0.246(0.175)	0.179(0.126)
LIROS	0.175(0.122)	0.240(0.171)	0.175(0.122)
LIROS*	0.167(0.117)	0.222(0.158)	0.166(0.117)
LIROMA	0.180(0.126)	0.248(0.176)	0.181(0.127)
LIROMA*	0.167(0.117)	0.228(0.162)	0.167(0.118)
Operational	0.174(0.122)		
TAN	0.195(0.137)		
EMPIRIMA	0.168(0.118)	0.216(0.153)	0.168(0.118)
NOCORR	0.393(0.321)		

TABLE IV
SAME AS TABLE II BUT FOR DAYTIME DATA

σ_m	GAMSRE	GMODIR	GMAO
MPM85	12.73	13.72	12.53
MPM85*	11.83	12.65	11.66
MPM85*CO	12.66	13.64	12.47
MPM93	12.43	13.35	12.24
MPM93L1	12.34	13.25	12.15
MPM93L2	12.49	13.42	12.29
MPM93*	11.51	12.27	11.35
LIROS	11.17	11.89	11.0205
LIROS*	10.34	10.92	10.22
LIROMA	11.60	12.38	11.44
LIROMA*	10.74	11.38	10.60
Operational	10.80		
TAN	12.12		
EMPIRIMA	10.59	11.13	10.48
NOCORR	6.20		

and daytime is different, but the data dispersion is following the same pattern. The conclusions that we are drawing from the analysis are identical for nighttime and daytime data.

The improvement of different MPM versions follows the chronological order. MPM93 lowers the dispersion with respect to MPM85. LIROS and LIROMA are leading to a significant improvement with respect to MPM93. LIROS being better than LIROMA is not totally surprising as [27] only provides an expression for the foreign-broadened continuum, so combining it with the self-broadened continuum in [25] is not expected to give perfect results. There was no certainty that the chronological improvement for models supposed to fit a large range of frequency would follow the same tendency at a given wavelength, but it seems to be the case here. For MPM85, using the complete version (MPM85) or the corrected version (MPM85*CO) leads to an identical dispersion. For MPM93, the most accurate parameterization of water vapor continuum comes with the 1470-GHz line, then using the “standard” 1780-GHz line, and then the 2200-GHz line. As we can see, the exact details of parameterization are important even for small variations of the same model.

Using GMODIR is systematically less accurate than using AMSR-E or GMAO alone. This was expected as the uncertainty on integrated water vapor content is higher for MODIS (4 kg/m² [29]) than for AMSR-E (0.57 kg/m² [30]). The accuracy of GMAO water vapor is interesting as we would expect it to do well in regions where there are large numbers of radio soundings assimilated or in the tropics where the variability in space and time is relatively low. However, as we can see in Fig. 5, the observations are not specifically shifted toward the tropics. Moreover, oceanic areas typically offer few radio-sounding observations. It is therefore very encouraging particularly considering the simple procedure that we used to extrapolate the thermodynamic profile at the surface level, and we are planning to conduct further investigation to better understand to which extent using the models is a viable option when correcting water vapor absorption.

TAN parameterizing the attenuation in terms of AMSR-E IWVP shows a lower dispersion than GAMSRE with usual MPM85 and MPM93. In this paper, we do not address the exact importance of profile shape. However, as TAN is more accurate than most of the correction using GMODIR as a constraint, it seems to be more important to obtain a precise value of IWVP

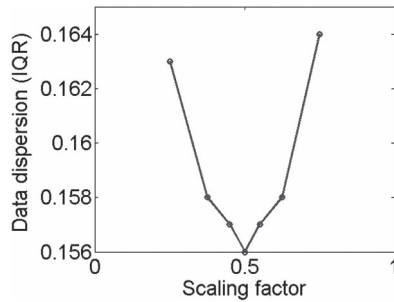


Fig. 8. Data dispersion as in Table I as a function of the scaling factor in the self-broadened continuum expression in [25].

than a correct profile shape. The good behavior of TAN is promising for future improvements using a polynomial function of IWVP, as suggested by several authors [1], [31]. This kind of simple parameterization possesses the great advantage of reducing the computing power needed, and further developments would be useful to correct water vapor absorption for an important amount of data in a short amount of time.

The operational product (Operational) using Liebe 89 model and ECMWF data shows a low level of dispersion. This was a little bit unexpected as using the integrated water vapor amount a few hundred meters higher than sea level should not lead to a good correction. A possible explanation is that the low dispersion would come from statistical error compensation occurring when using a water vapor content lower than it is in reality and a water vapor correction factor higher than it is.

This is consistent with the reduced models being systematically better than the complete version. However, the goal of the reduced model was to improve computation speed [3]. The addition of the correction factor [3] allows it to stay close from the complete version and was obviously not aimed to decrease its accuracy. As the only change between the complete and the reduced models is the removal of several absorption lines, all of this would suggest the water vapor correction when using MPM is too high at 94 GHz.

LIROS* performs extremely well, but the problem in water vapor correction seems to be linked to the continuum absorption [27] and not the absorptions lines. As the absorptions lines of MPM93 have been compared to spectroscopic measurements, using all of them and modifying the continuum contribution are more physically consistent than to remove several absorption lines.

This leads us to combine MPM93 with the theoretical work in [27] and then empirically search the lowest value of the dispersion for the self-broadened continuum expression in [25]. Dividing it by half as done in the EMPIRIMA model (see Annex A) offers the lowest dispersion (Fig. 8).

We think that using this model (EMPIRIMA) has more physical justification than using LIROS* until further theoretical work is performed to improve our knowledge of self-broadened continuum or absorption line shapes. There is a direct analogy between this result and the work performed by AMSR scientists using MPM85 for lower frequency. They stated “We find that very good agreement is obtained by reducing the self-broadening component of the water vapor continuum by a factor of 0.52” [31]. As a different model and a different

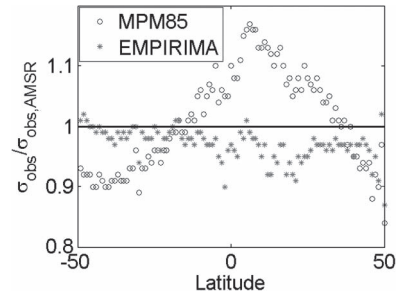


Fig. 9. Latitudinal variation of the ratio of effective normalized scattering cross section on the expected value retrieved from AMSR-E wind speed retrieval using two different models and GAMSRE.

frequency were involved, finding the same number may be due to other factors. However, the fact that they also needed to reduce this component is probably meaningful and would suggest that the self-broadening component being taken too high is a general statement. Furthermore, given the regular behavior of the continuum, one should expect high correlation between findings at 89 and 94 GHz. This is also supported by recent studies based on the data from the Department of Energy’s Atmospheric Radiation Measurement program [10], [11]. A necessary reduction of the self-broadening component by a factor of around 1.88 was evidenced [11] when scaling the monochromatic radiative transfer model to approximate the Rosenkranz continuum. Even if our finding is qualitatively consistent with those recent studies, caution is advised when comparing the exact numbers found as different frequencies are involved and the models used are not totally identical.

When the dispersion is lowered using the lidar measurement as a reference, it also increases the consistency with AMSR-E wind speed retrieval. There is a well-defined relationship between CloudSat normalized scattering cross section (corrected from water vapor absorption) and AMSR-E wind speed [1], [16]. This relationship allows one to retrieve an equivalent normalized scattering cross section $\sigma_{\text{obs,AMSR}}$ (function of wind speed W_{AMSR})

$$\sigma_{\text{obs,AMSR}} = f(W_{\text{AMSR}}). \quad (12)$$

It is then possible to study the latitudinal variations of the ratio of the observed radar normalized cross section σ_{obs} to $\sigma_{\text{obs,AMSR}}$. We retrieved this relationship at global scale for the same month of data (nighttime) that we used for the dispersion analysis. The results reported in Fig. 9 show a latitudinal variation of around 10% in mid-latitudes (50° S and 50° N) and around 20% around the Intertropical Convergence Zone (ITCZ) level at 5° N when using MPM85/GAMSRE. Using EMPIRIMA/GAMSRE shows a much stable behavior, reducing the difference in the tropics where much of the water vapor is observed (the latitude of the IWVP peak in August is corresponding to the ITCZ latitude). Some residual variations are observed but can be well explained by the expected error of AMSR-E wind speed (0.86 m/s).

This suggests consistency between our approach of using optical wavelength as a reference and the wind speed product retrieved by AMSR-E.

Overall, the difference between the maximum and minimum dispersion of this study (MPM85/GMODIR and EMPIRIMA/GAMSRE corrections) is 30% in terms of bias, and it is 78% in terms of IQR. Although the error bar differences in the water vapor retrieval between MODIS and AMSR-E are significant (assuming a mean content of 25 kg/m², the errors in IWVP coming from AMSR-E and MODIS are 2% and 16%, respectively), the choice of the atmospheric models is also critical to reduce the dispersion.

This work allows a precise error characterization of our optical thickness retrieval [15], [16]. When correcting CloudSat with EMPIRIMA/GAMSRE and using the full resolution (lidar shot to shot) of the data, the data dispersion corresponds to an error bar in an optical depth of 0.058 for nighttime measurement. Error bar has to be understood in the usual sense of the standard deviation of the Gaussian distribution (divided by two for optical thickness [16]) with the same IQR as retrieved in Table I. No water vapor correction leads to an error bar of 0.149. The improvement due to water vapor correction is then 0.09 in terms of optical depth error, which is quite significant. For our optical depth retrieval, this number is a good estimation of the expected error, as a global bias can be easily corrected. Indeed, the clearest conditions should have an aerosol optical depth close to zero and cannot be negative, which offers a guidance to correct any global bias. Performing an average of the data lowers this dispersion. When we perform a 5-km average of CALIPSO and CloudSat data, the error bar is expected to reduce to 0.015. During daytime, the error is higher because lidar calibration variations and increased noise should be added to this number and the expected error on optical depth due to data dispersion (shot to shot) is increased to 0.059.

IV. CONCLUSION

A combination of optical (lidar) and microwave (CloudSat/AMSR-E) instruments has been used to check water vapor correction. We have created an empirical model allowing us to minimize the dispersion of CALIPSO/CloudSat collocated ocean surface observations. The dispersion is further reduced when AMSR-E water vapor retrieval is used as a constraint for GMAO water vapor profile. We identify here two models allowing us to optimize retrievals in which we are proposing to use a new empirical derivation (EMPIRIMA) over a reduced model (LIROS*). Our result on the parameterization change of self-broadening contribution is consistent to what has been derived by the AMSR-E science team for lower frequencies.

The results of this study are significant for the assessment of the overall calibration of the CloudSat radar instrument and all the retrievals obtained from the CPR measurements. From a CALIPSO perspective, as this study opens the way for a totally new domain of application for a space backscatter lidar, it would be premature to try to predict the whole extent and the exact specifics of its implications.

In terms of general perspectives, we have identified an important potential of the synergetic A-train observations to critically analyze the contribution of water vapor continuum in the 3-mm wavelength domain. As the A-train is performing measurements in the whole possible range of temperature and

pressure observed on earth, it is a useful tool to characterize model accuracy. One further aspect that is worth considering pertains to the use of these models into radiative transfer calculations and retrievals from passive sensors: As shown in Fig. 1, the conclusions drawn in this analysis for 94 GHz appear to have relevance also for 89- and 85-GHz passive channels given the high correlation across the frequencies. While such analysis is beyond the scope of this paper, we envision that the findings described here should be considered also within that context.

APPENDIX A PARAMETERS OF THE MPM

To facilitate future utilization of the EMPIRIMA model, we are providing it hereinafter in the same formalism as [4]. As only absorption has been studied, only the part contributing to the imaginary refractive index will be described.

The attenuation α (in decibels per kilometer) is equal to

$$\alpha = 0.1820N'\nu + \alpha_{Ma} + \alpha_{EMPIRIMA}. \quad (A1)$$

N' is the imaginary part of the refractive index N whose derivation is coming from the model in [4]. It contains the following parameterization for the foreign-broadened water vapor continuum [27]. ν is the radar frequency (in gigahertz).

$$\alpha_{Ma} = 1.5915 \times 10^{-9} e \cdot p \cdot \theta^{4.982} \nu^{2.059} \quad (A2)$$

where the dry air pressure p , the partial pressure of water vapor e , and the reciprocal temperature $\theta = 300/T$ (T being the temperature in kelvins) are used. We are using the following expression for the self-broadened continuum (half the parameterization in [25] once the line shape difference has been taken into account)

$$\alpha_{EMPIRIMA} = \nu^2 \theta^3 C_s e^2 \quad (A3)$$

$$C_s = 3.783 \times 10^{-8} \theta^{4.5}. \quad (A4)$$

The part of N containing an imaginary part can be expressed as (we want to stress again that the real nondispersive term is not included in this expression)

$$N = N_n + \sum S_{O_2} F_{O_2} + \sum S_{H_2O} F_{H_2O}. \quad (A5)$$

It is the summation of the different-spectral-line contribution and the nonresonant oxygen term contribution N_n .

For O₂ and H₂O, the line strengths are respectively

$$S_{O_2} = \frac{a_1}{\nu_k} p \theta^3 \exp(a_2(1 - \theta)) \quad (A6)$$

$$S_{H_2O} = \frac{b_1}{\nu_k} e \theta^{3.5} \exp(b_2(1 - \theta)). \quad (A7)$$

Those line strengths are weighted by the following shape function (Van Vleck–Weisskopf):

$$F_{O_2} = \nu \left[\frac{(1 - i\Delta_{O_2})}{\nu_k - \nu - i\Gamma_{O_2}} - \frac{1 + i\Delta_{O_2}}{\nu_k + \nu + i\Gamma_{O_2}} \right] \quad (A8)$$

$$F_{H_2O} = \nu \left[\frac{1}{\nu_k - \nu - i\Gamma_{H_2O}} - \frac{1}{\nu_k + \nu + i\Gamma_{H_2O}} \right]. \quad (A9)$$

TABLE V
SPECTROSCOPIC COEFFICIENTS OF O₂ LINES IN AIR (LIEBE 93 REFERRED TO HERE AS MPM 93)

Center freq. ν_k	Strength		Width		Overlap	
	a_1	a_2	a_3	a_4	a_5	a_6
GHz	kHz/hPa		MHz/hPa		hPa ⁻¹	
50.474238	9.4e-8	9.694	0.89	0.8	0.24e-3	0.79e-3
50.987749	2.46e-7	8.694	0.91	0.8	0.22e-3	0.78e-3
51.503350	6.08e-7	7.744	0.94	0.8	0.197e-3	0.774e-3
52.021410	1.414e-6	6.844	0.97	0.8	0.166e-3	0.764e-3
52.542394	3.102e-6	6.004	0.99	0.8	0.136e-3	0.751e-3
53.066907	6.410e-6	5.224	1.02	0.8	0.131e-3	0.714e-3
53.595749	1.2470e-5	4.484	1.05	0.8	0.230e-3	0.584e-3
54.13	2.280e-5	3.814	1.07	0.8	0.335e-3	0.431e-3
54.671159	3.9180e-5	3.194	1.10	0.8	0.374e-3	0.305e-3
55.221367	6.3160e-5	2.624	1.13	0.8	0.258e-3	0.339e-3
55.783802	9.5350e-5	2.119	1.17	0.8	-0.166e-3	0.705e-3
56.264775	5.4890e-5	0.015	1.73	0.8	0.39e-3	-0.113e-3
56.363389	1.34400e-4	1.66	1.2	0.8	-0.297e-3	0.753e-3
56.968206	1.76300e-4	1.26	1.24	0.8	-0.416e-3	0.742e-3
57.612484	2.14100e-4	0.915	1.28	0.8	-0.613e-3	0.697e-3
58.323877	2.38600e-4	0.626	1.33	0.8	-0.205e-3	0.051e-3
58.44659	1.45700e-4	0.084	1.52	0.8	0.748e-3	-0.146e-3
59.164207	2.40400e-4	0.391	1.39	0.8	-0.722e-3	0.266e-3
59.590983	2.11200e-4	0.212	1.43	0.8	0.765e-3	-0.090e-3
60.306061	2.12400e-4	0.212	1.45	0.8	-0.705e-3	0.081e-3
60.434776	2.46100e-4	0.391	1.36	0.8	0.697e-3	-0.324e-3
61.150560	2.50400e-4	0.626	1.31	0.8	0.104e-3	-0.067e-3
61.800154	2.29800e-4	0.915	1.27	0.8	0.57e-3	-0.761e-3
62.411215	1.93300e-4	1.26	1.23	0.8	0.36e-3	-0.777e-3
62.486260	1.51700e-4	0.083	1.54	0.8	-0.498e-3	0.097e-3
62.997977	1.50300e-4	1.665	1.20	0.8	0.239e-3	-0.768e-3
63.568518	1.08700e-4	2.115	1.17	0.8	0.108e-3	-0.706e-3
64.127767	7.3350e-5	2.620	1.13	0.8	-0.311e-3	-0.332e-3
64.678903	4.6350e-5	3.195	1.10	0.8	-0.421e-3	-0.298e-3
65.224071	2.7480e-5	3.815	1.07	0.8	-0.375e-3	-0.423e-3
65.764772	1.5300e-5	4.485	1.05	0.8	-0.267e-3	-0.575e-3
66.302091	8.009e-6	5.225	1.02	0.8	-0.168e-3	-0.7e-3
66.836830	3.946e-6	6.005	0.99	0.8	-0.169e-3	-0.735e-3
67.369598	1.832e-6	6.845	0.97	0.8	-0.200e-3	-0.744e-3
67.900867	8.01e-7	7.745	0.94	0.8	-0.228e-3	-0.753e-3
68.431005	3.300e-7	8.695	0.92	0.8	-0.240e-3	-0.760e-3
68.960311	1.280e-7	9.695	0.90	0.8	-0.250e-3	-0.765e-3
118.750343	9.450e-5	0.009	1.63	0.8	-0.036e-3	0.009e-3
368.498350	6.790e-6	0.049	1.92	0.2	0.0	0.0
424.763124	6.380e-5	0.044	1.93	0.2	0.0	0.0
487.249370	2.350e-5	0.049	1.92	0.2	0.0	0.0
715.393150	9.960e-6	0.145	1.81	0.2	0.0	0.0
773.839675	6.710e-5	0.130	1.82	0.2	0.0	0.0
834.145330	1.800e-5	0.147	1.81	0.2	0.0	0.0

See Table V and Table VI for the central frequency ν_k value. It contains the nonresonant O₂ spectra parameters
The width Γ and overlap Δ expressions are as follows:

$$\Gamma_{O_2} = a_3 10^{-3} (p\theta^{a_4} + 1.1e\theta) \quad (A10)$$

$$\Delta_{O_2} = (a_5 + a_6\theta)p\theta^{0.8} \quad (A11)$$

$$\Gamma_{H_2O} = b_3 10^{-3} (b_4 e\theta^{b_6} + p\theta^{b_5}). \quad (A12)$$

$$S_0 = 6.14 \times 10^{-5} p\theta^2 \quad (A14)$$

$$F_0 = -\frac{\nu}{\nu + i\Gamma_0} \quad (A15)$$

where the relaxation frequency is

$$\Gamma_0 = 0.56 \times 10^{-3} (p + e)\theta^{0.8}. \quad (A16)$$

The nonresonant oxygen term contribution N_n can then be expressed as

$$N_n = S_0 F_0 + iS_n F_n. \quad (A13)$$

Moreover, the pressure-induced N₂ absorption parameters are

$$F_n = \frac{\nu}{1 + 1.9 \times 10^{-5} \nu^{1.5}} \quad (A17)$$

$$S_n = 1.40 \times 10^{-12} p^2 \theta^{3.5}. \quad (A18)$$

TABLE VI
SPECTROSCOPIC COEFFICIENTS OF H₂O LINES IN AIR (LIEBE 93)

Center freq. ν_k GHz	Strength		Width			
	b_1 kHz/hPa	b_2	b_3 MHz/hPa	b_4	b_5	b_6
22.235080	0.01130	2.143	2.811	4.80	0.69	1.00
67.803960	0.00012	8.735	2.858	4.93	0.69	0.82
119.995940	0.00008	8.356	2.948	4.78	0.70	0.79
183.310091	0.24200	0.668	3.050	5.30	0.64	0.85
321.225644	0.00483	6.181	2.303	4.69	0.67	0.54
325.152919	0.14990	1.540	2.783	4.85	0.68	0.74
336.222601	0.00011	9.829	2.693	4.74	0.69	0.61
380.197372	1.15200	1.048	2.873	5.38	0.54	0.89
390.134508	0.00046	7.350	2.152	4.81	0.63	0.55
437.346667	0.00650	5.050	1.845	4.23	0.60	0.48
439.150812	0.09218	3.596	2.100	4.29	0.63	0.52
443.018295	0.01976	5.050	1.860	4.23	0.60	0.50
448.001075	1.03200	1.405	2.632	4.84	0.66	0.67
470.888947	0.03297	3.599	2.152	4.57	0.66	0.65
474.689127	0.12620	2.381	2.355	4.65	0.65	0.64
488.491133	0.02520	2.853	2.602	5.04	0.69	0.72
503.568532	0.00390	6.733	1.612	3.98	0.61	0.43
504.482692	0.00130	6.733	1.612	4.01	0.61	0.45
547.676440	0.97010	0.114	2.600	4.50	0.70	1.00
552.020960	1.47700	0.114	2.600	4.50	0.70	1.00
556.936002	48.74000	0.159	3.210	4.11	0.69	1.00
620.700807	0.50120	2.200	2.438	4.68	0.71	0.68
645.866155	0.00713	8.580	1.800	4.00	0.60	0.50
658.005280	0.03022	7.820	3.210	4.14	0.69	1.00
752.033227	23.96000	0.396	3.060	4.09	0.68	0.84
841.053973	0.00140	8.180	1.590	5.76	0.33	0.45
859.962313	0.01472	7.989	3.060	4.09	0.68	0.84
899.306675	0.00605	7.917	2.985	4.53	0.68	0.90
902.616173	0.00426	8.432	2.865	5.10	0.70	0.95
906.207325	0.01876	5.111	2.408	4.70	0.70	0.53
916.171582	0.83410	1.442	2.670	4.78	0.70	0.78
923.118427	0.00869	10.22	2.900	5.00	0.70	0.80
970.315022	0.89720	1.920	2.550	4.94	0.64	0.67
987.926764	13.21000	0.258	2.985	4.55	0.68	0.90

APPENDIX B

NOTE ON THE DETERMINATION OF THE SATURATION WATER VAPOR PRESSURE

The different versions of the MPM [3], [4] are using different formulations to calculate the saturation water vapor pressure e_S and translate the relative humidity to water vapor partial pressure. The associated equations are for MPM85

$$e_S = \frac{10^3}{41.51} \theta^5 10^{-(9.834\theta-10)} \quad (B1)$$

and for MPM93

$$e_S = 2.408 \cdot 10^{11} \theta^5 \exp(-22.644\theta). \quad (B2)$$

e_S is expressed in hectopascals. Even if the different formulations give close results, it introduces small differences between the models that may slightly affect the comparison, and we replaced the previous expressions by the Bolton formula for all models to retrieve the saturation water vapor pressure. Its expression as a function of the temperature T_C in Celsius is

$$e_S = 6.112 \exp\left(\frac{17.67T_C}{T_C + 243.5}\right). \quad (B3)$$

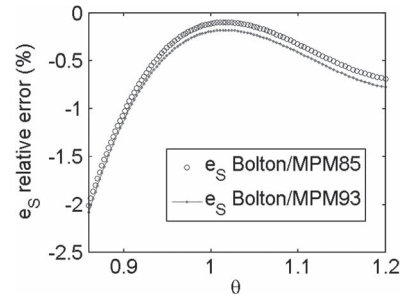


Fig. 10. Relative error of saturation water vapor pressure e_S between the formulations of Bolton, MPM85, and MPM93 as a function of the reciprocal temperature θ .

The relative difference of water vapor saturation pressure as a function of reciprocal temperature between Bolton, MPM85, and MPM93 formulas is shown in Fig. 10.

Different formulations exist in the literature to retrieve e_S . Among them, we can cite the one by Murphy and Koop [32]

$$e_S = 10^{-2} \exp\left(\begin{aligned} &54.842763 - \frac{6763.22}{T} \\ &-4.21 \ln(T) + 0.000367T \\ &+ \tanh[0.0415(T-218.8)] \left(\begin{aligned} &53.878 - \frac{1331.22}{T} \\ &-9.44523 \ln(T) \\ &+ 0.014025T \end{aligned} \right) \end{aligned} \right) \quad (B4)$$

$$\log_{10} e_S = \left(\begin{array}{l} 10.79574 \left(1 - \frac{273.16}{T} \right) - 5.02800 \log_{10} \frac{T}{273.16} \\ + 1.50475 \cdot 10^{-4} \left[1 - 10^{8.2969 \left(1 - \frac{T}{273.16} \right)} - 0.42873 \cdot 10^{-3} \left\{ 1 - 10^{4.76955 \left(1 - \frac{273.16}{T} \right)} \right\} \right] \\ + 0.78614 \end{array} \right) \quad (B5)$$

or the one by Goff and Gratch [33] as in [34], which is recommended by the World Meteorological Organization, given by (B5), shown at the top of the page.

We tested formulations (B3)–(B5) for one of the versions of the MPM [LIROS*] with no change in the final dispersion. This suggests that the difference of dispersion induced by changing the water vapor saturation formulation is small and beyond the scope of this study. Therefore, adopting the Bolton formula is not considered an issue.

ACKNOWLEDGMENT

The authors would like to thank the ICARE French Archive (<http://www.icare.univ-lille1.fr/>) Center for the MODerate-resolution Imaging Spectroradiometer (MODIS) collocation (CALTRACK product), the NASA and CNES for their support and data availability for the CALIPSO, CloudSat, MODIS, and AMSR-E project, and two anonymous reviewers for their useful comments. The contributions by Simone Tanelli were performed at the Jet Propulsion Laboratory, California Institute of Technology, under contract with the National Aeronautics and Space Administration for the CloudSat mission. Special kudos must go to H. J. Liebe for his outstanding contribution to science and for the creation of the millimeter-wave propagation models.

REFERENCES

- [1] S. Tanelli, S. L. Durden, E. Im, K. S. Pak, D. G. Reinke, P. Partain, J. M. Haynes, and R. T. Marchand, "Cloudsat's cloud profiling radar after two years in orbit: Performance, calibration and processing," *IEEE Trans. Geosci. Remote Sens.*, vol. 46, no. 11, pp. 3560–3573, Nov. 2008.
- [2] H. J. Liebe, "MPM—An atmospheric millimeter-wave propagation model," *Int. J. Infrared Millim. Waves*, vol. 10, no. 6, pp. 631–650, Jun. 1989.
- [3] H. J. Liebe, "An updated model for millimeter wave propagation in moist air," *Radio Sci.*, vol. 20, no. 5, pp. 1069–1089, May 1985.
- [4] H. J. Liebe, G. A. Hufford, and M. G. Cotton, "Propagation modeling of moist air and suspended water/ice particles at frequencies below 1000 GHz," in *Proc. AGARD Meeting Atmos. Propag. Effects Through Natural Man-Made Obscurants Visible MM-Wave Radiation*, May 1993, pp. 3/1–3/11.
- [5] L. Li, G. M. Heymsfield, L. Tian, and P. E. Racette, "Measurements of ocean surface backscattering using an airborne 94-GHz cloud radar—Implication for calibration of airborne and spaceborne W-band radars," *J. Atmos. Ocean. Technol.*, vol. 22, no. 7, pp. 1033–1045, Jul. 2005.
- [6] S. D. Miller and G. L. Stephens, "CloudSat instrument requirements as determined from ECMWF forecasts of global cloudiness," *J. Geophys. Res.*, vol. 106, no. 16, pp. 17713–17733, Aug. 2001.
- [7] M. J. McGill, L. Li, W. D. Hart, G. M. Heymsfield, D. L. Hlavka, P. E. Racette, L. Tian, M. A. Vaughan, and D. M. Winker, "Combined lidar–radar remote sensing: Initial results from CRYSTAL-FACE," *J. Geophys. Res.*, vol. 109, no. D7, pp. D07203-1–D07203-13, Apr. 2004.
- [8] A. Protat, D. Bouniol, J. Delanoe, P. T. May, A. Plana-Fattori, A. Hasson, E. O' Connor, U. Gorsdorf, and A. J. Heymsfield, "Assessment of CloudSat reflectivity measurements and ice cloud properties using ground-based and airborne cloud radar observations," *J. Atmos. Ocean. Technol.*, vol. 26, no. 9, pp. 1717–1741, Sep. 2009.
- [9] R. Marchand, T. Ackerman, E. R. Westwater, S. A. Clough, K. Cady-Pereira, and J. C. Liljegen, "An assessment of microwave absorption models and retrievals of cloud liquid water using clear-sky data," *J. Geophys. Res.*, vol. 108, no. D24, pp. 4773–4783, Dec. 2003.
- [10] D. D. Turner, U. Loehnert, M. Cadeddu, S. Crewell, and A. Vogelmann, "Modifications to the water vapor continuum in the microwave suggested by ground-based 150 GHz observations," *IEEE Trans. Geosci. Remote Sens.*, vol. 47, no. 10, pp. 3326–3337, Oct. 2009.
- [11] V. H. Payne, E. J. Mlawer, K. E. Cady-Pereira, and J.-L. Moncet, "Water vapor continuum absorption in the microwave," *IEEE Trans. Geosci. Remote Sens.*, vol. 49, pp. 2194–2208, Jun. 2011.
- [12] J. H. Haynes, T. S. L'Ecuyer, G. L. Stephens, S. D. Miller, C. M. Mitrescu, and S. Tanelli, "Rainfall retrieval over the ocean using spaceborne high-frequency cloud radar," *J. Geophys. Res.*, vol. 114, pp. D00A22-1–D00A22-18, Feb. 2008.
- [13] G. L. Stephens, D. G. Vane, S. Tanelli, E. Im, S. Durden, M. Rokey, D. Reinke, P. Partain, G. G. Mace, R. Austin, T. S. L'Ecuyer, J. Haynes, M. Lebsock, K. Suzuki, D. Waliser, D. Wu, J. Kay, A. Gettleman, Z. Wang, and R. Marchand, "CloudSat mission: Performance and early science after the first year of operation," *J. Geophys. Res.*, vol. 113, no. D15, pp. D00A1-1–D00A18-18, Dec. 2008.
- [14] D. M. Winker, J. Pelon, J. A. Coakley, Jr., S. A. Ackerman, R. J. Charlson, P. R. Colarco, P. Flamant, Q. Fu, R. Hoff, C. Kittaka, T. L. Kubar, H. LeTret, M. P. McCormick, G. Megie, L. Poole, K. Powell, C. Trepte, M. A. Vaughan, and B. A. Wielicki, "The CALIPSO mission: A global 3D view of aerosols and clouds," *Bull. Amer. Meteorol. Soc.*, vol. 91, no. 9, pp. 1211–1229, Sep. 2010.
- [15] D. Jossset, J. Pelon, A. Protat, and C. Flamant, "New approach to determine aerosol optical depth from combined CALIPSO and CloudSat ocean surface echoes," *Geophys. Res. Lett.*, vol. 35, no. 10, pp. L10805-1–L10805-5, May 2008.
- [16] D. Jossset, J. Pelon, and Y. Hu, "Multi-instrument calibration method based on a multiwavelength ocean surface model," *IEEE Geosci. Remote Sens. Lett.*, vol. 7, no. 1, pp. 195–199, Jan. 2010.
- [17] T. Meissner and F. J. Wentz, "The complex dielectric constant of pure and sea water from microwave satellite observations," *IEEE Trans. Geosci. Remote Sens.*, vol. 42, no. 9, pp. 1836–1849, Sep. 2004.
- [18] X. Quan and E. S. Fry, "Empirical equation for the index of refraction of seawater," *Appl. Opt.*, vol. 34, no. 18, pp. 3477–3480, Jun. 1995.
- [19] Y. Liu, M. Y. Su, X. H. Yan, and W. T. Liu, "The mean-square slope of ocean surface waves and its effect on radar backscatter," *J. Atmos. Ocean. Technol.*, vol. 17, no. 8, pp. 1092–1108, Aug. 2000.
- [20] R. G. Valenzuela, "Theories for the interaction of electromagnetic and oceanic waves—A review," *Boundary Layer Meteorol.*, vol. 13, no. 1–4, pp. 61–85, Jan. 1978.
- [21] Y. Hu, K. Stamnes, M. Vaughan, J. Pelon, C. Weimer, D. Wu, M. Cisewski, W. Sun, P. Yang, B. Lin, A. Omar, D. Flittner, C. Hostetler, C. Trepte, D. Winker, G. Gibson, and M. Santa-Maria, "Sea surface wind speed estimation from space-based lidar measurements," *Atmos. Chem. Phys.*, vol. 8, no. 13, pp. 3593–3601, Jul. 2008.
- [22] P. Koepke, "Effective reflectance of oceanic whitecaps," *Appl. Opt.*, vol. 23, no. 11, pp. 1816–1824, Nov. 1984.
- [23] C. Flamant, J. Pelon, D. Hauser, C. Quentin, W. M. Drennan, F. Gohin, B. Chapron, and J. Gourrion, "Analysis of surface wind speed and roughness length evolution with fetch using a combination of airborne lidar and radar measurements," *J. Geophys. Res.*, vol. 108, no. C3, pp. 8058–8084, Feb. 2003.
- [24] Y. J. Kaufman, A. Smirnov, B. N. Holben, and O. Dubovik, "Baseline maritime aerosol: Methodology to derive the optical thickness and scattering properties," *Geophys. Res. Lett.*, vol. 28, no. 17, pp. 3251–3254, Sep. 2001.
- [25] P. W. Rosenkranz, "Water vapor microwave continuum absorption: A comparison of measurements and models," *Radio Sci.*, vol. 33, no. 4, pp. 919–928, Jul./Aug. 1998.
- [26] P. W. Rosenkranz, "Correction to "Water vapor microwave continuum absorption: A comparison of measurements and models"," *Radio Sci.*, vol. 34, no. 4, p. 1025, Jul./Aug. 1999.

- [27] Q. Ma and R. H. Tipping, "A simple analytical parameterization for the water vapor millimeter wave foreign continuum," *J. Quant. Spectrosc. Radiat. Transf.*, vol. 82, no. 1–4, pp. 517–531, Nov. 2003.
- [28] S. A. Clough, F. X. Kneizys, and R. W. Davies, "Line shape and the water vapor continuum," *Atmos. Res.*, vol. 23, no. 3/4, pp. 229–241, Oct. 1989.
- [29] S. W. Seemann, J. Li, W. P. Menzel, and L. E. Gumley, "Operational retrieval of atmospheric temperature, moisture, and ozone from MODIS infrared radiances," *J. Appl. Meteorol.*, vol. 42, no. 8, pp. 1072–1091, Aug. 2003.
- [30] AMSR-E/Aqua L2B and L3 Ocean Products. [Online]. Available: http://nsidc.org/data/docs/daac/ae_ocean_products.gd.html
- [31] F. Wentz and T. Meissner, "AMSR Ocean Algorithm. Algorithm Theoretical Basis Document Version 2," Remote Sensing Systems, Santa Rosa, CA, 2000.
- [32] D. M. Murphy and T. Koop, "Review of the vapour pressures of ice and supercooled water for atmospheric applications," *Q. J. R. Meteorol. Soc.*, vol. 131, no. 608, pp. 1539–1565, Apr. 2005.
- [33] J. A. Goff and S. Gratch, "Low-pressure properties of water from -160° to 212° F," *J. Trans. Amer. Soc. Heat. Vent. Eng.*, vol. 52, pp. 95–122, 1946.
- [34] O. A. Alduchov and R. E. Eskridge, "Improved Magnus form approximation of saturation vapor pressure," *J. Appl. Meteorol., Notes Correspondence*, vol. 35, no. 4, pp. 601–609, Apr. 1996.

Authors' photographs and biographies not available at the time of publication.